JOURNAL OF THEORETICAL
AND APPLIED MECHANICS
63, 2, pp. 289–306, Warsaw 2025
https://doi.org/10.15632/jtam-pl/200379

GLOBAL BEHAVIORS OF PARAMETERIZED SOLUTION DOMAIN AND BASINS OF ATTRACTION OF STAR HERRINGBONE GEAR TRANSMISSION SYSTEM

He LIN[1,2*], Jiamin GUO[1], Yingjie LI[1], Xiaole CHENG[1], Ling HONG[2]

[1] *School of Mechanical and Electrical Engineering, Xi'an Polytechnic University, Xi'an, 710048, China*
[2] *State Key Laboratory for Strength and Vibration of Mechanical Structures, Xi'an Jiaotong University, Xi'an 710049, China*

*corresponding author, *linhe@xpu.edu.cn*

The analysis of global behaviors is quite essential for the prediction of the potential dynamical vibration of the geared system. A novel meshing stiffness formula approximated to rectangular wave was proposed utilizing an odd harmonic superposition, the distribution maps of the parameterized solution domain and basin of attraction of the star herringbone gear transmission system were calculated containing various periodic regions and then validated. The analysis of the joint probability density indicates that transformations occurred on the portrait structure of attractors during the evolution into chaos. In addition, with discretization techniques and cell mapping methodology, the two-dimensional parameterized solution domain, as well as overall distributions of periodic and chaotic domains hidden in the basins of attraction were identified. Subsequently, the stochasticity of the damping ratio produced in normal distribution is analyzed, which presents that the attractor will experience perturbations before reaching a steady-state, while the periodicity of the attractor is significantly weakened. By the comparison of evolution behaviors, the distributions of periodic basin of attraction have little variations, but it caused some scattered periodic cells which mixed in the original domains, resulting in the deterioration of the steady-state to the system.

Keywords: time-varying meshing stiffness; parameterized solution domain; basin of attraction; joint probability density function; stochasticity.

Articles in JTAM are published under Creative Commons Attribution 4.0 International.
Unported License https://creativecommons.org/licenses/by/4.0/deed.en.
By submitting an article for publication, the authors consent to the grant of the said license.

Nomenclature

b – backlash,
b_c – nominal scale,
c – damping,
k – stiffness,
k_m – average meshing stiffness,
p_{ij} – joint probability density function,
$pi1$, $pi2$ – left and right side of the planetary gear i, respectively,
r – base circle radius,
$r1$, $r2$ – left and right side of ring gear, respectively,
$s1$, $s2$ – left and right side of sun gear, respectively,
u – dimensionless displacement,
u_{sp11}, $\dot{u}_{sp11}$ – dimensionless meshing displacement and velocity, respectively,
x, y – displacement along the X-axis and Y-axis, respectively,
E – amplitude of transmission error,
F – engagement force,
I – rotational inertia,
M – mass,
N_p – number of planetary gears,

T – torque,
U_i – uniformly distributed random number,
α_t, β – pressure and helical angle, respectively,
ε – stiffness fluctuation coefficient,
θ – angular displacement,
ξ – damping ratio,
φ, φ_0 – pressure, helical, phase angle, and initial phase angle, respectively,
ω – meshing frequency,
Θ – point sets.

1. Introduction

The star herringbone gear transmission system belongs to a power split gear dynamical machinery, which is normally applied in the situations that have extremely high-speed or high-power demands, such as warships, airplanes, gas turbines, even heavy machines and so forth. Its power transmission is from the sun gear to the planetary gear then converges by the internal ring gear, which could have remarkable advantages, such as quite high power density and the large transmission ratio. Compared with the planetary gear mechanism, the star herringbone gear transmission system adopts a fixed-axis gear train and possesses even better structural strength (Hong *et al.*, 2022; Arian & Taghvaei, 2021). However, the prominent issues deal with the problem of existing various vibrations on a conventional gear transmission that is also the concern of the technical research topics which the star herringbone gear transmission system encounters, especially the disclosure of its parametric domains and basins of attraction turns out to be particularly crucial for monitoring the dynamical behavior details, identifying the unstable dynamic regions or predicting the evolution processes of vibration more comprehensively (Li *et al.*, 2018).

As for now, many of the literatures regarding a gear system focusing on dynamical investigation can be mainly classified as a local analysis, that is, trying to compute dynamic solutions of the vibration, to analyze the stability of the response or even to study the influence of a parameter on vibrations. This kind of a numerical method has produced rich achievements during the previous exploration of gear dynamics. Wang *et al.* (2020) investigated the vibration of the GTF aero-engine star gear-rotor coupling system, and analyzed the gradual transformation mechanism of the bifurcation phenomenon. Marafona *et al.* (2024) studied the gear design optimization problem to minimize dynamic excitation by implementing the genetic algorithm (GA). Xiang *et al.* (2020) obtained the global bifurcation diagram of multi-stage gear transmission by altering the bifurcation parameter. Tang *et al.* (2020) presented an analytical model of time-varying support stiffness based on the Hertz contact theory, their calculations indicate that the planetary gear system with an external node engagement will enter uncertainties and cause chaos nearby the resonance frequency. Nevertheless, many studies on the excitation behavior of a gear system mainly investigate the primary unidirectional dimension. In the matter of the dynamical modeling of the star herringbone gear transmission system, apart from considering the conventional excitations, such as, the time-varying meshing stiffness and external load fluctuation, then the designated strong nonlinear influencing factor such as backlash has also been taken into account. But diverse excitations are mutually related or coupled with each other to determine the system vibration properties, on the other hand, the stochasticity present in the parameter excitations also has a significant impact on the long-term global behaviors. If one wants to thoroughly figure out the internal mechanism between these factors versus the global evolution of dynamical solutions or clarify the hierarchical domain distribution between excitation channels, the exploration of solution domain will be essential and feasible. The research on the solution domain of the star herringbone gear transmission system mainly focuses on the region of a parametric solution domain and the analysis of the global characteristics of attractors in the basin of attraction, so as to track the evolutionary behaviors of the attractor and state basins from a given phase space and acquire the spatial microscopic details of global solutions.

In global analysis, the cell mapping technique (Wang *et al.*, 2023; Koh *et al.*, 2021) has been mostly used for the investigation of dynamical issues, as a well-known computation algorithm based on the evolutionary probability vector, it is also suitable for exploring meshed gear-tooth pair dynamics with strong nonlinearity. Besides, it is also able to track out the potential vibration situation of the system due to its ability to comprehensively evaluate the attractive region and the emergence location of chaos. Gyebrószki *et al.* (2017), Ma *et al.* (2020), Yue *et al.* (2019), and Zhang *et al.* (2019) have published relevant researches and applications involving different fields adopting that methodology, and also discussed the development tendency and technical challenges. Tang *et al.* (2011) utilized a graph cell mapping method to achieve the global solution sets of a spur gear system with a single degree of freedom (DOF) earlier. Mo *et al.* (2022) calculated the phase trajectory of the discrete cell on the Poincaré section, and observed the influence of the initial state on dynamic behaviors. Farshidianfar *et al.* (2014) and Saghafi *et al.* (2016) developed the homoclinic bifurcation and chaotic migration of the gear system in the global domain based on the Melnikov method, and accurately predicted the location of the chaotic parameter band. According to the regional discretization investigation, Lin *et al.* (2021) studied the bifurcation evolutions of a power-split gear transmission under multiple dynamical excitations. With the combination of simple cell mapping and the escape time algorithm, Gou *et al.* (2015) captured the variety of coupled vibration information of the torsional vibration gear system on the two-parameter plane.

Advantageous dynamical status conditions are meaningful to improve the stability of various gear transmission systems. In this study, the global nonlinear characteristics of the star herringbone gear transmission system from the view of multiple dimensions have been investigated, the dynamic parameters subjected to stochastic disturbance causing global variational effects were considered as well. Associated with the joint probability density function and the domain discretization technology, the determination criteria of the boundary and domain of attraction are deduced theoretically, the borderline structure and attractor behavior of the solution domain under two parameterized dynamic excitations of speed and input power are computed, and the stability and transition pattern of the attractive domain in the meshing vibration state space are simulated too. The researches show that the vibration sensitivity of the system to the initial states can be weakened and excellent steady-state characteristics can be obtained by reasonable configuring the operating conditions of the initial parameters, thereby providing the reference for the optimization of global domains and resonance parameter designs of the star herringbone gear transmission system.

2. Modeling of the star herringbone gear transmission system

The translational-torsional dynamical model of the star herringbone gear transmission system with backlash is established by employing the lumped mass method, as shown in Fig. 1. Wherein, θ_s, θ_{pi} $(i = 1, 2, 3)$, and θ_r denote the rotational vibration displacements of the sun gear, the i-th planetary gear and the ring gear around the Z-axis direction, respectively; x_s, x_{pi}, x_r, y_s, y_{pi}, and y_r are the translational vibration displacements of the sun gear, the i-th planetary gear and the internal ring gear measured along the X-axis and Y-axis direction, respectively; Fm is the meshing force between the teeth along the line of action. In the model presented in Fig. 1b, the planetary carrier is fixed to the frame without any displacement, so the rotational and translational vibrations of the carrier could be ignored. All herringbone gears in the entire system should be with a standard involute tooth profile, which are regarded as the splicing of two helical gears with opposite helical angle and the same physical property, regardless of the sliding or sliding friction between meshing teeth. Meanwhile, the Euler beam unit is connected between the left and right gear tooth.

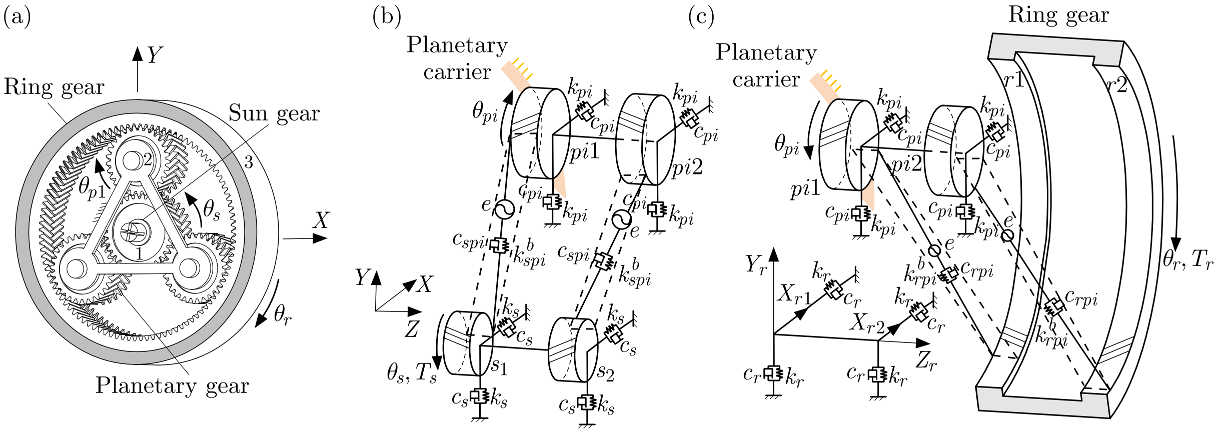

Fig. 1. (a) Dynamic schematics of star herringbone gear transmission system; (b) dynamic model between sun gear and planetary gear; (c) dynamic model between planetary gear and ring gear.

Considering the symmetry in the circumferential of the system, in order to characterize the dynamic details between component gears, the meshing translational-torsional dynamical model shown in Figs. 1b and 1c are established for only one of the planetary gears. The mass nodes $s1$ and $s2$ represent the left and right side of helical teeth of the sun gear, $pi1$ and $pi2$ represent the left side and right side of the planetary gear i $(i = 1, 2, 3)$, similarly, $r1$ and $r2$ represent the two side helical teeth of the ring gear, respectively.

In light of the analysis of the gear meshing movement, the dynamical differential governing equations of vibration of the system could be established.

The dynamical differential equations of motion of the left side of the sun gear can be expressed as Eq. (2.1). The dynamical differential equations of motion of the right side of the sun gear can be expressed as Eq. (2.2). The dynamical differential equations of motion of the left side of the planetary gear pi can be expressed as Eq. (2.3). The dynamical differential equations of motion of the right side of the planetary gear pi can be expressed as Eq. (2.4). The dynamical differential equations of motion of the left side of the internal ring gear can be expressed as Eq. (2.5). The dynamical differential equations of motion of the right side of the internal ring gear can be expressed as Eq. (2.6).

$$
\begin{aligned}
I_{s1}\ddot{\theta}_{s1} &= -\sum_{i=1}^{3} F_{spi1}\, r_{s1} \cos\beta_1 + T_s, \\
M_{s1}\ddot{x}_{s1} &= -\sum_{i=1}^{3} F_{spi1} \sin\varphi_{spi} \cos\beta_1 - k_s x_{s1} - c_s \dot{x}_{s1}, \\
M_{s1}\ddot{y}_{s1} &= -\sum_{i=1}^{3} F_{spi1} \cos\varphi_{spi} \cos\beta_1 - k_s y_{s1} - c_s \dot{y}_{s1},
\end{aligned}
\tag{2.1}
$$

$$
\begin{aligned}
I_{s2}\ddot{\theta}_{s2} &= -\sum_{i=1}^{3} F_{spi2}\, r_{s2} \cos\beta_2, \\
M_{s2}\ddot{x}_{s2} &= -\sum_{i=1}^{3} F_{spi2} \sin\varphi_{spi} \cos\beta_2 - k_s x_{s2} - c_s \dot{x}_{s2}, \\
M_{s2}\ddot{y}_{s2} &= -\sum_{i=1}^{3} F_{spi2} \cos\varphi_{spi} \cos\beta_2 - k_s y_{s2} - c_s \dot{y}_{s2},
\end{aligned}
\tag{2.2}
$$

$$
\begin{aligned}
I_{pi1}\ddot{\theta}_{pi1} &= -F_{spi1}\, r_{pi1} \cos\beta_1 + F_{rpi1}\, r_{pi1} \cos\beta_1, \\
M_{pi1}\ddot{x}_{pi1} &= F_{spi1} \sin\varphi_{spi} \cos\beta_1 - F_{rpi1} \sin\varphi_{rpi} \cos\beta_1 - k_{pi}x_{pi1} - c_{pi}\dot{x}_{pi1}, \\
M_{pi1}\ddot{y}_{pi1} &= F_{spi1} \cos\varphi_{spi} \cos\beta_1 + F_{rpi1} \cos\varphi_{rpi} \cos\beta_1 - k_{pi}y_{pi1} - c_{pi}\dot{y}_{pi1},
\end{aligned}
\tag{2.3}
$$

$$
\begin{aligned}
I_{pi1}\ddot{\theta}_{pi2} &= -F_{spi2}\, r_{pi2} \cos\beta_2 + F_{rpi2}\, r_{pi2} \cos\beta_2, \\
M_{pi2}\ddot{x}_{pi2} &= F_{spi2} \sin\varphi_{spi} \cos\beta_2 - F_{rpi2} \sin\varphi_{rpi} \cos\beta_2 - k_{pi}x_{pi2} - c_{pi}\dot{x}_{pi2}, \\
M_{pi1}\ddot{y}_{pi2} &= F_{spi2} \cos\varphi_{spi} \cos\beta_2 + F_{rpi2} \cos\varphi_{rpi} \cos\beta_2 - k_{pi}y_{pi2} - c_{pi}\dot{y}_{pi2},
\end{aligned}
\tag{2.4}
$$

$$
\begin{aligned}
I_{r1}\ddot{\theta}_{r1} &= -\sum_{i=1}^{3} F_{rpi1}\, r_{r1} \cos\beta_1, \\
M_{r1}\ddot{x}_{r1} &= -\sum_{i=1}^{3} F_{rpi1} \sin\varphi_{spi} \cos\beta_1 - k_s x_{r1} - c_s\dot{x}_{r1}, \\
M_{r1}\ddot{y}_{r1} &= -\sum_{i=1}^{3} F_{rpi1} \cos\varphi_{spi} \cos\beta_1 - k_s y_{r1} - c_s\dot{y}_{r1},
\end{aligned}
\tag{2.5}
$$

$$
\begin{aligned}
I_{r2}\ddot{\theta}_{r2} &= -\sum_{i=1}^{3} F_{rpi2}\, r_{r2} \cos\beta_2 + T_r, \\
M_{r2}\ddot{x}_{r2} &= -\sum_{i=1}^{3} F_{rpi2} \sin\varphi_{spi} \cos\beta_2 - k_s x_{r2} - c_s\dot{x}_{r2}, \\
M_{r2}\ddot{y}_{r2} &= -\sum_{i=1}^{3} F_{rpi2} \cos\varphi_{spi} \cos\beta_2 - k_s y_{r2} - c_s\dot{y}_{r2}.
\end{aligned}
\tag{2.6}
$$

From Eq. (2.1) to Eq. (2.6), I indicates the rotational inertia; M denotes the equivalent mass, where $M = I/r^2$; β_1 and β_2 are the helical angle of the herringbone gears, assuming that left-hand rotation is positive and right-hand rotation is negative, then there the relationship occurs $\beta_2 = -\beta_1$. F_{spi} is the meshing force between the sun gear and the planetary gear, and F_{rpi} is the meshing force between the planetary gear and the ring gear, given as

$$
\begin{aligned}
F_{spi} &= k_{spi} f\left(x_{spi}, b\right) + c\dot{x}_{spi}, \\
F_{rpi} &= k_{rpi} f\left(x_{rpi}, b\right) + c\dot{x}_{rpi},
\end{aligned}
\tag{2.7}
$$

where k_{spi} and k_{rpi} are the meshing stiffness between the sun gear and the planetary gear, and c_{spi}, c_{rpi} are the meshing damping between the planetary gear and the ring gear, respectively; $f(x, b)$ describes the expression of the backlash; b is the backlash; x_{spi} and x_{rpi} are the relative displacements along the line of action between meshing pairs.

Here, we define the time-varying meshing stiffness by an approximate square wave, which can be built by the abbreviated function $k(t)$ and the mean meshing stiffness k_m, when we take the first three orders of j ($j = 1$, $j = 2$, $j = 3$) and draw the superimposed harmonic waveform in Fig. 2a:

$$
k'(t) = \frac{2k_m}{\pi}\left[\sin(\omega t) + \frac{1}{3}\sin(3\omega t) + \ldots + \frac{1}{j}\sin(j\omega t) + \ldots\right],
\tag{2.8}
$$

where ($j = 1, 3, 5, ..., 2n + 1$), E represents the square wave amplitude. The first three order harmonic waveforms of meshing stiffness can be plotted, respectively, in Fig. 2b.

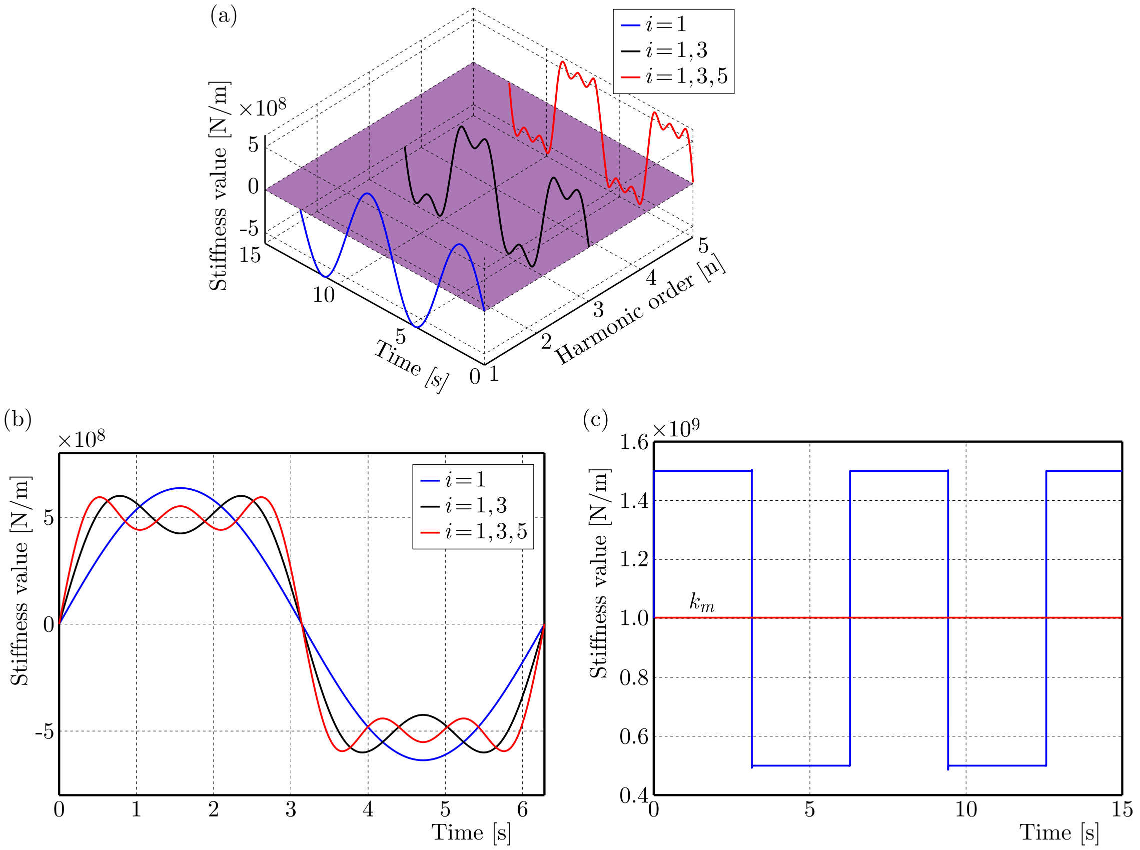

Fig. 2. (a) Superposition of the first three order harmonic waveform of time-varying meshing stiffness; (b) harmonic waveform superposition of the first three orders (1 period); (c) approximate model of the time-varying meshing stiffness.

In Fig. 2c, then the time-varying meshing stiffness of the gear system can be expressed by the Fourier series as

$$k(t) = k_m + \varepsilon k'(t) = k_m + \varepsilon \frac{2k_m}{\pi} \sum_{i=1}^{\infty} \left(\sin \left(\frac{1}{j} \omega t + \varphi_0 \right) \right), \qquad (j = 1, 3, 5, ..., 2n + 1), \quad (2.9)$$

where ω is the meshing frequency, and ε represents the fluctuation coefficient of the time-varying meshing stiffness; φ_0 denotes the initial phase angle, and defines the initial phase angle φ_{spi} and φ_{rpi}, respectively:

$$\begin{aligned} \varphi_{spi} &= \alpha_t - 2\pi(i-1)/N_p, \quad (i = 1, 2, 3), \\ \varphi_{rpi} &= \alpha_t + 2\pi(i-1)/N_p, \quad (i = 1, 2, 3). \end{aligned} \quad (2.10)$$

The meshing damping related to the meshing stiffness is derived, and given as Eq. (2.11). The nonlinear function of the backlash can be expressed as Eq. (2.12):

$$c_{spi} = 2\xi \sqrt{k_m / M_{esp}}, \quad (2.11)$$

$$f(x, b) = \begin{cases} x - b/2 & x > b/2, \\ 0 & -b/2 \le x \le b/2, \\ x + b/2 & x < -b/2, \end{cases} \quad (2.12)$$

where ξ is the meshing damping ratio, M_{esp} denotes the equivalent mass of mating gears between the sun gear and the planetary gear.

Then along the line of action, x_{spi1} and x_{spi2} are the relative meshing displacements between the sun gear and the i-th planetary gear; similarly, x_{rpi1} and x_{rpi2} denote the i-th planetary gear and the ring gear, which can be separately expressed as follows:

$$\begin{aligned}
x_{spi1} &= [(x_{s1} - x_{pi1}) \sin\varphi_{spi} + (y_{s1} - y_{pi1}) \cos\varphi_{spi} \\
&\quad + (r_{s1}\theta_{s1} + r_{pi1}\theta_{pi1})] \cos\beta_1 - e_{i1}(t), \\
x_{spi2} &= [(x_{s2} - x_{pi2}) \sin\varphi_{spi} + (y_{s2} - y_{pi2}) \cos\varphi_{spi} \\
&\quad + (r_{s2}\theta_{s2} + r_{pi2}\theta_{pi2})] \cos\beta_2 - e_{i2}(t), \\
x_{rpi1} &= [(x_{pi1} - x_{r1}) \sin\varphi_{spi} + (y_{r1} - y_{pi1}) \cos\varphi_{spi} \\
&\quad + (r_{r1}\theta_{r1} - r_{pi1}\theta_{pi1})] \cos\beta_1 - e_{i3}(t), \\
x_{rpi2} &= [(x_{pi2} - x_{r2}) \sin\varphi_{spi} + (y_{r2} - y_{pi2}) \cos\varphi_{spi} \\
&\quad + (r_{r2}\theta_{r2} - r_{pi2}\theta_{pi2})] \cos\beta_2 - e_{i4}(t),
\end{aligned} \tag{2.13}$$

where $e_{ij}(t) = E\sin(\omega t + \varphi_0)$ $(i = 1, 2, 3;\ j = 1, 2, 3, 4)$, $e_{ij}(t)$ is the comprehensive transmission error, and E indicates the amplitude. Taking the second derivative to Eq. (2.13) and substituting it into Eqs. (2.1)–(2.6), then the differential equations adopted for eliminating rigid body displacement can be obtained as follows:

$$\begin{aligned}
\ddot{x}_{spi1} &= \Bigg[(\ddot{x}_{s1} - \ddot{x}_{pi1}) \sin\varphi_{spi} + (\ddot{y}_{s1} - \ddot{y}_{pi1}) \cos\varphi_{spi} + r_{s1}T_s/I_{s1} \\
&\quad - \sum_{i=1}^{3} F_{spi1} \cos\beta_1/M_{s1} + \cos\beta_1 \left(F_{rpi1} - F_{spi1}\right)/M_{pi1}\Bigg] \cos\beta_1 - \ddot{e}_{i1}(t), \\
\ddot{x}_{spi2} &= \Bigg[(\ddot{x}_{s2} - \ddot{x}_{pi2}) \sin\varphi_{spi} + (\ddot{y}_{s2} - \ddot{y}_{pi2}) \cos\varphi_{spi} \\
&\quad + \left(-\sum_{i=1}^{3} F_{spi2}/M_{s2} + \left(F_{rpi2} - F_{spi2}\right)/M_{pi2}\right) \cos\beta_2\Bigg] \cos\beta_2 - \ddot{e}_{i2}(t), \\
\ddot{x}_{rpi1} &= \Bigg[(\ddot{x}_{pi1} - \ddot{x}_{r1}) \sin\varphi_{spi} + (\ddot{y}_{r1} - \ddot{y}_{pi1}) \cos\varphi_{spi} \\
&\quad + \left(-\sum_{i=1}^{3} F_{rpi1}/M_{r1} + \left(F_{spi1} - F_{rpi1}\right)/M_{pi1}\right) \cos\beta_1\Bigg] \cos\beta_1 - \ddot{e}_{i3}(t), \\
\ddot{x}_{rpi2} &= \Bigg[(\ddot{x}_{pi2} - \ddot{x}_{r2}) \sin\varphi_{spi} + (\ddot{y}_{r2} - \ddot{y}_{pi2}) \cos\varphi_{spi} + r_{r1}T_r/I_{r1} \\
&\quad - \sum_{i=1}^{3} F_{rpi2} \cos\beta_2/M_{r2} + \cos\beta_2 \left(F_{spi2} - F_{rpi2}\right)/M_{pi2}\Bigg] \cos\beta_2 - \ddot{e}_{i4}(t).
\end{aligned} \tag{2.14}$$

With the help of above expressions, the dynamical equations of the entire system in a unified form after eliminating rotational rigid displacement is simplified as

$$[\mathbf{M}]\,\ddot{\mathbf{X}} + [\mathbf{C}]\,\dot{\mathbf{X}} + [\mathbf{K}]\,\mathbf{f}\left(\mathbf{X}, \mathbf{b}\right) = \mathbf{F}, \tag{2.15}$$

where $\mathbf{X}$ represents the displacement vector; $\mathbf{M}$, $\mathbf{C}$, $\mathbf{K}$, and $\mathbf{F}$, respectively, indicate the mass matrix, damping matrix, stiffness matrix, and load vector, each of them is given as

$$\mathbf{X} = [x_{spi1},\, x_{spi2},\, x_{rpi1},\, x_{rpi2},\, x_{s1},\, y_{s1},\, x_{s2},\, y_{s2},\, x_{pi1},\, y_{pi1},\, x_{pi2},\, y_{pi2},\, x_{r1},\, y_{r1},\, x_{r2},\, y_{r2}]^{\mathrm{T}}, \tag{2.16}$$

$$\mathbf{M}=\begin{bmatrix}\mathbf{E}_{2\times2} & 0_{2\times2} & \mathbf{A} & -\mathbf{A} & 0_{2\times4}\\ 0_{2\times2} & \mathbf{E}_{2\times2} & 0_{2\times4} & \mathbf{B} & -\mathbf{B}\\ 0_{2\times2} & 0_{2\times2} & \mathbf{m}_1 & 0_{2\times4} & 0_{2\times4}\\ 0_{2\times2} & 0_{2\times2} & \mathbf{m}_2 & 0_{2\times4} & 0_{2\times4}\\ 0_{2\times2} & 0_{2\times2} & 0_{2\times4} & \mathbf{m}_3 & 0_{2\times4}\\ 0_{2\times2} & 0_{2\times2} & 0_{2\times4} & \mathbf{m}_4 & 0_{2\times4}\\ 0_{2\times2} & 0_{2\times2} & 0_{2\times4} & 0_{2\times4} & \mathbf{m}_5\\ 0_{2\times2} & 0_{2\times2} & 0_{2\times4} & 0_{2\times4} & \mathbf{m}_6\end{bmatrix},\qquad \mathbf{A}=\begin{bmatrix}-a_1 & -a_2 & 0 & 0\\ 0 & 0 & -a_3 & -a_4\end{bmatrix},$$

$$\mathbf{m}_1=\begin{bmatrix}m_{s1} & 0 & 0 & 0\\ 0 & m_{s1} & 0 & 0\end{bmatrix},\qquad \mathbf{m}_2=\begin{bmatrix}m_{s2} & 0 & 0 & 0\\ 0 & m_{s2} & 0 & 0\end{bmatrix},$$

$$\mathbf{m}_3=\begin{bmatrix}m_{pi1} & 0 & 0 & 0\\ 0 & m_{pi1} & 0 & 0\end{bmatrix},\qquad \mathbf{m}_4=\begin{bmatrix}m_{pi2} & 0 & 0 & 0\\ 0 & m_{pi2} & 0 & 0\end{bmatrix},$$

$$\mathbf{m}_5=\begin{bmatrix}m_{r1} & 0 & 0 & 0\\ 0 & m_{r1} & 0 & 0\end{bmatrix},\qquad \mathbf{m}_6=\begin{bmatrix}m_{r2} & 0 & 0 & 0\\ 0 & m_{r2} & 0 & 0\end{bmatrix}, \tag{2.17}$$

$$\mathbf{K}\backslash\mathbf{C}=\begin{bmatrix}\mathbf{D}_1 & \mathbf{D}_2 & 0_{2\times2} & 0_{2\times2} & 0_{2\times2} & 0_{2\times2} & 0_{2\times2} & 0_{2\times2}\\ \mathbf{D}_3 & \mathbf{D}_4 & 0_{2\times2} & 0_{2\times2} & 0_{2\times2} & 0_{2\times2} & 0_{2\times2} & 0_{2\times2}\\ \mathbf{D}_5 & 0_{2\times2} & \mathbf{K_s} & 0_{2\times2} & 0_{2\times2} & 0_{2\times2} & 0_{2\times2} & 0_{2\times2}\\ 0_{2\times2} & \mathbf{D}_6 & 0_{2\times2} & \mathbf{K_s} & 0_{2\times2} & 0_{2\times2} & 0_{2\times2} & 0_{2\times2}\\ \mathbf{D}_7 & \mathbf{D}_8 & 0_{2\times2} & 0_{2\times2} & \mathbf{K}_{pi} & 0_{2\times2} & 0_{2\times2} & 0_{2\times2}\\ \mathbf{D}_9 & \mathbf{D}_{10} & 0_{2\times2} & 0_{2\times2} & 0_{2\times2} & \mathbf{K}_{pi} & 0_{2\times2} & 0_{2\times2}\\ 0_{2\times2} & \mathbf{D}_{11} & 0_{2\times2} & 0_{2\times2} & 0_{2\times2} & 0_{2\times2} & \mathbf{K}_r & 0_{2\times2}\\ 0_{2\times2} & \mathbf{D}_{12} & 0_{2\times2} & 0_{2\times2} & 0_{2\times2} & 0_{2\times2} & 0_{2\times2} & \mathbf{K}_r\end{bmatrix}, \tag{2.18}$$

$$\mathbf{F}=\left[\left(r_{s1}T_s\cos\beta_1\right)/I_{s1}\quad 0_{1\times2}\quad \left(r_{s1}T_r\cos\beta_2\right)/I_{r2}\quad 0_{1\times12}\right]^{\mathrm{T}},$$

where

$$\mathbf{D}_1=\begin{bmatrix}\left(\sum\limits_{i=1}^{3}\varGamma_{spi}/m_{s1}+\varGamma_{spi}/m_{pi1}\right)\cos^2\beta_1 & 0\\ 0 & \left(\sum\limits_{i=1}^{3}\varGamma_{spi}/m_{s2}+\varGamma_{spi}/m_{pi2}\right)\cos^2\beta_2\end{bmatrix},$$

$$\mathbf{D}_2=\begin{bmatrix}-\left(\varGamma_{rpi}\cos^2\beta_1\right)/m_{pi1} & 0\\ 0 & -\left(\varGamma_{rpi}\cos^2\beta_2\right)/m_{pi2}\end{bmatrix},$$

$$\mathbf{D}_3=\begin{bmatrix}-\left(\varGamma_{spi}\cos^2\beta_1\right)/m_{pi1} & 0\\ 0 & -\left(\varGamma_{spi}\cos^2\beta_2\right)/m_{pi2}\end{bmatrix},$$

$$\mathbf{D}_4=\begin{bmatrix}\left(\sum\limits_{i=1}^{3}\varGamma_{rpi}/m_{r1}+\varGamma_{rpi}/m_{pi1}\right)\cos^2\beta_1 & 0\\ 0 & \left(\sum\limits_{i=1}^{3}\varGamma_{rpi}/m_{r2}+\varGamma_{rpi}/m_{pi2}\right)\cos^2\beta_2\end{bmatrix},$$

$$\mathbf{D}_5=\begin{bmatrix}\sum\limits_{i=1}^{3}\varGamma_{spi}a_1 & 0\\ \sum\limits_{i=1}^{3}\varGamma_{spi}a_2 & 0\end{bmatrix},\qquad \mathbf{D}_6=\begin{bmatrix}0 & \sum\limits_{i=1}^{3}\varGamma_{spi}a_1\\ 0 & \sum\limits_{i=1}^{3}\varGamma_{spi}a_2\end{bmatrix},\qquad \mathbf{D}_7=\begin{bmatrix}-\varGamma_{spi}a_1 & 0\\ -\varGamma_{spi}a_2 & 0\end{bmatrix},$$

$$\mathbf{D}_8 = \begin{bmatrix} \varGamma_{rpi}b_1 & 0 \\ -\varGamma_{rpi}b_2 & 0 \end{bmatrix}, \qquad \mathbf{D}_9 = \begin{bmatrix} 0 & -\varGamma_{spi}a_3 \\ 0 & -\varGamma_{spi}a_4 \end{bmatrix}, \qquad \mathbf{D}_{10} = \begin{bmatrix} \varGamma_{rpi}b_3 & 0 \\ -\varGamma_{rpi}b_4 & 0 \end{bmatrix},$$

$$\mathbf{D}_{11} = \begin{bmatrix} -\sum\limits_{i=1}^{3} \varGamma_{rpi}b_1 & 0 \\ \sum\limits_{i=1}^{3} \varGamma_{rpi}b_2 & 0 \end{bmatrix}, \qquad \mathbf{D}_{12} = \begin{bmatrix} -\sum\limits_{i=1}^{3} \varGamma_{rpi}b_3 & 0 \\ \sum\limits_{i=1}^{3} \varGamma_{rpi}b_4 & 0 \end{bmatrix},$$

$$\mathbf{K}_s = \varGamma_s\mathbf{E}_{2\times2}, \qquad \mathbf{K}_{pi} = \varGamma_{pi}\mathbf{E}_{2\times2}, \qquad \mathbf{K}_r = \varGamma_r\mathbf{E}_{2\times2},$$

where

$$\mathbf{E}_{2\times2} = \begin{bmatrix} 1 & 0 \\ 0 & 1 \end{bmatrix},$$

$$\begin{aligned} &a_1 = \sin\varphi_{spi}\cos\beta_1, && a_2 = \cos\varphi_{spi}\cos\beta_1, && a_3 = \sin\varphi_{spi}\cos\beta_2, && a_4 = \cos\varphi_{spi}\cos\beta_2, \\ &b_1 = \sin\varphi_{rpi}\cos\beta_1, && b_2 = \cos\varphi_{rpi}\cos\beta_1, && b_3 = \sin\varphi_{rpi}\cos\beta_2, && b_4 = \cos\varphi_{rpi}\cos\beta_2. \end{aligned}$$

To simplify the computation of aforementioned matrices, the symbol $\varGamma$ is introduced, $\varGamma$ would be substituted by stiffness or damping according to Eq. (2.15). The following Eq. (2.19) is demonstrating the substitution of $\varGamma$ in the matrix $\mathbf{D}_1$ by means of stiffness k_{spi}:

$$\mathbf{D}_1 = \begin{bmatrix} \Big(\sum\limits_{i=1}^{3} k_{spi}/m_{s1} + k_{spi}/m_{pi1}\Big)\cos^2\beta_1 & 0 \\ 0 & \Big(\sum\limits_{i=1}^{3} k_{spi}/m_{s2} + k_{spi}/m_{pi2}\Big)\cos^2\beta_2 \end{bmatrix}, \tag{2.19}$$

$$\omega_n = \sqrt{k_m\,(1/M_s + 1/M_{pi})}. \tag{2.20}$$

Additionally, k_s, k_{pi}, and k_r are the support stiffness of the sun gear, planetary gear and ring gear, respectively; similarly, c_s, c_{pi}, and c_r represent their damping correspondingly.

During the numerical computation of Eq. (2.15), a dimensionless operation is required to avoid the convergence problem due to the huge differences in the order of magnitude of the polynomial coefficient. Therefore, the dimensionless nominal scale parameter is defined as Eq. (2.20), where M_s and M_{pi} indicate the equivalent masses of the sun gear and the planetary gear, separately. Once the nominal time scale ω_n and displacement scale b_c, $b_c = 100\times10^{-6}$ m are defined, then the time τ, vibration displacement u and backlash $\bar{b}$ with normalized dimensions can be derived as $\tau = \omega_n t$, $u(\tau) = x(t)/b_c$, and $\bar{b} = b/b_c$.

3. Global behaviors of parameterized solution domain and basins of attraction

3.1. Solutions inside the parameterized plane

The followings and Table 1 provide the essential dynamical parameters of the star herringbone gear transmission system. For instance, the amount of planetary gears is 3; all the gear modulus is 4 mm; the installation angle α_{pi} $(i = 1,2,3)$ of each planetary gear is 0, $2\pi/3$, and $4\pi/3$; the normal pressure angle α_n is 20°, and the base helical angle β_b is 22.5°. The mean stiffness km is 2×10^9 N/m; the support stiffness k is 1×10^6 N/m; the stiffness fluctuation coefficient ε is 0.1; the meshing damping ratio ξ is 0.1; the power is 3000 kW, and the backlash b is set 0.1 mm.

The two-dimensional parametric domain is composed of the horizontal parameter μ_j $(j = 1,2,...,j)$ and the vertical parameter λ^i $(i = 1,2,...,i)$, both directions are discretized into a certain number of cells, c_{ij} represents a single cell (see Fig. 3). Next, combining with Eq. (3.1) and adopting the Runge–Kutta method to compute the dynamical differential equations in Eq. (2.20). Parameterized cells that have the same periodic solution constitute a periodic domain

Table 1. Partial major parameters of the gears.

	Sun gear	Planetary gear	Ring gear
Number of teeth Z	36	32	100
Mass m [kg]	5.30	4.50	16.08
Moment of interia I [$\mathrm{kg \cdot m^2}$]	0.0226	0.0149	0.6564

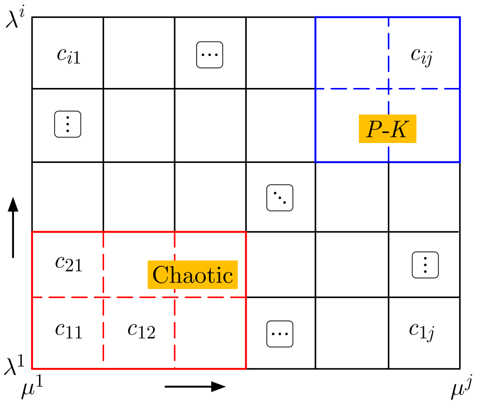

Fig. 3. Cell discretization of two-dimensional parametric domain.

of period-K (P-K), K is the periodic state, and called P-K motion. Similarly, chaotic solution can also be calculated.

In global analysis of the parameterized plane, each discretized cell represents an exact value of an excitation parameter for numerical calculation, and the initial state (0, 0) is brought into the differential equations of motion. The mapping iteration starts from time $\tau = 0$, and 4 adjacent mapping points of the attractor in state space are extracted from the Poincaré section, then compared with the criteria value of $\varepsilon_1 = 1.0 \times 10^{-3}$, and $\varepsilon_2 = 1.0 \times 10^{-4}$, respectively, here the ε_2 determines the periodic state of the attractor domains in calculation.

For point sets $\Theta \in R^n$, n is the dimension of the system, and Θ is the set of all points on the Poincaré section achieved by mappings. Assuming $X(i)$ is one of the points in the Θ, accordingly, $X^{(i)} \in P$ ($i = 1, 2, ..., k$), k is the quantity of points in the set Θ. Here, Y is another point on the Poincaré section, and Y_j ($j = 1, 2, ..., n$) is the j-th component of Y, then we can define the 2-norm between point Y and point set Θ as

$$\rho(Y, \Theta) = \min\left(\mathrm{dis}\,(Y, X^{(i)})\right), \qquad i = 1, 2, ..., k, \tag{3.1}$$

where

$$\mathrm{dis}\,(Y, X^{(i)}) = \max\left|Y_j - X_j^{(i)}\right|, \qquad j = 1, 2, ..., n. \tag{3.2}$$

If point Y and the point set Θ satisfy the following expression, $\rho(Y, \Theta) < \varepsilon$.

Consequently, it can be determined that point Y falls within the domain of attraction composed of the point set A. If the $\rho(Y, \Theta) < \varepsilon$ is still not satisfied, that means there might exist a chaotic attractor under the present parameter. To ensure that result, preset 5 extra mappings to the potential chaotic attractor.

In Fig. 4, which is divided into 300×300 regular cells in the parameterized plane, after discretization and iteration, the two-dimensional solution domains could be plotted out. The distribution of various dynamic parameter domains is identified with the aid of series of discrete cells. One can clearly see that the period-doubling bifurcation imbedded in the parametric plane, which is presented while the rotational speed raises from 4000 rpm to 20000 rpm.

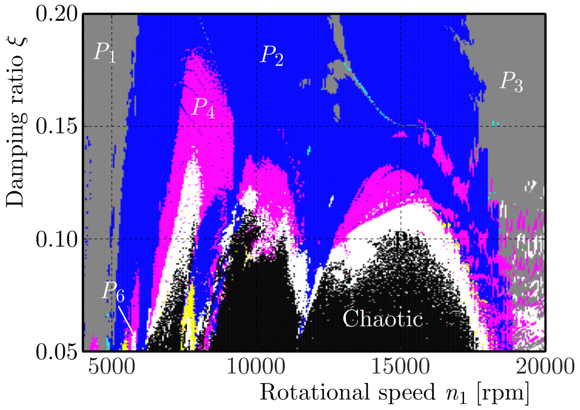

Fig. 4. Two-dimensional plane of parameterized solution domain.

A parametric cell at (8000, 0.15) is select from Fig. 4 and its phase portrait and the Poincaré diagram are computed as shown in red color in Fig. 5. Then chaotic attractor is also analyzed in the same way, at this point, the phase trajectory in chaotic state exhibits a little bit local repeated with winding, and the fractal characteristic of the mapping points on the Poincaré section are obvious. The period-4 attractor now with slightly larger size maintains a certain distance away from the chaotic attractor. That implies the period-4 attractor will move down if the speed or damping ratio varies properly into the chaotic domain. Accordingly, on the selection of parameters from solution cells, a chaotic vibration can be also eliminated by driving into the periodic domains.

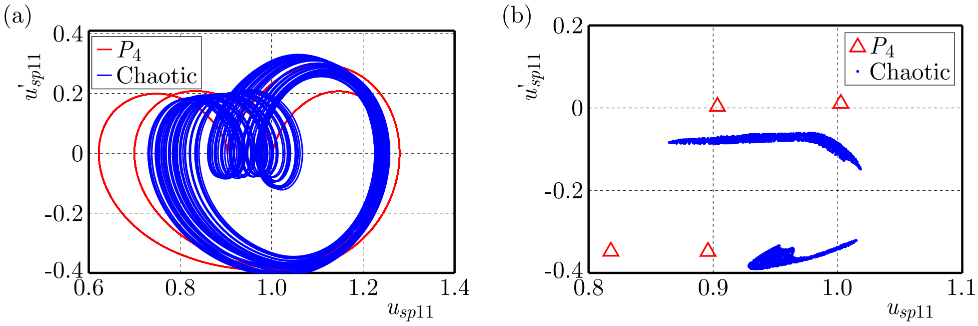

Fig. 5. (a) Phase portrait and (b) Poincaré section of attractors.

One of the global analysis is to study the movement behaviors of the attractor. The projection of the phase trajectory will play a major role. Next, to explore the behavior of the attractor transformation by using the joint probability density function $P(X, Y)$. We define the two-dimensional discrete variable (X, Y), all possible points in the target region Ω could be defined by (x, y), then it has Eq. (3.3).

In the study of the star herringbone gear transmission system, the joint distribution of two-dimensional discrete variables is defined as Eq. (3.4):

$$P((X,Y)\in\Omega)=\iint_A f(x,y), \qquad \text{for all} \quad \Omega, \tag{3.3}$$

$$p_{ij}=P\{X=u_{sp11}, Y=\dot{u}_{sp11}\}. \tag{3.4}$$

Then, by using the Monte Carlo method (Dreeben *et al.*, 1998) the joint probability density function is calculated. For the period-4 attractor, the vertical peak representing the probability density of the attractor at the intersection of the Poincaré section. In Fig. 6, four convex peaks

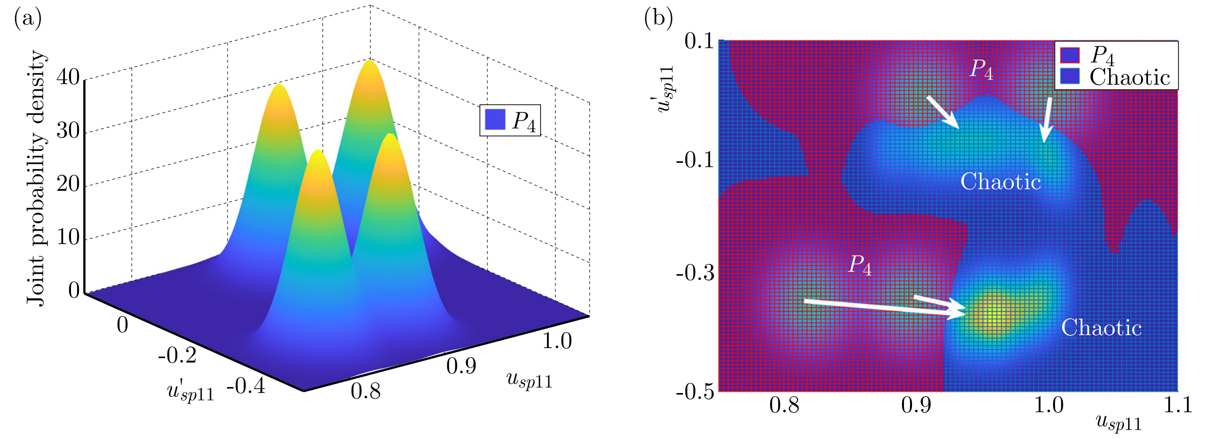

Fig. 6. (a) Joint probability density of period-4 attractor; (b) the evolution of attractor from period-4 to chaos.

between each of them are almost equal proving that this attractor has only four harmonic periods and no other coexisting attractors. Afterwards, as the damping ratio decreases to 0.05, we see the period-4 attractor has started to move down and approach to the chaotic attractor gradually.

3.2. Validation of parameterized solution domains

The local domain of interest which consists of speed and power with the finite field of [4000, 20000] × [1500, 4000]. The solutions reveal information on the steady-state oscillations in a more overall way on the plane (Fig. 7), and mainly including period-1, period-2, period-4, multi-period, and chaotic parameterized regions. The various regions suggest the differences of steady-state result if under excitation, particularly, more uncertainties will appear adjacent to the borderline. During the increasing of horizontal speed, the periodic state changes frequently, which indicates the system behavior is sensitive to the variation of the sun gear velocity, however, while in the vertical direction at 4000 r/min, the dynamic domain seems to keep period-1 motion with the increase of power.

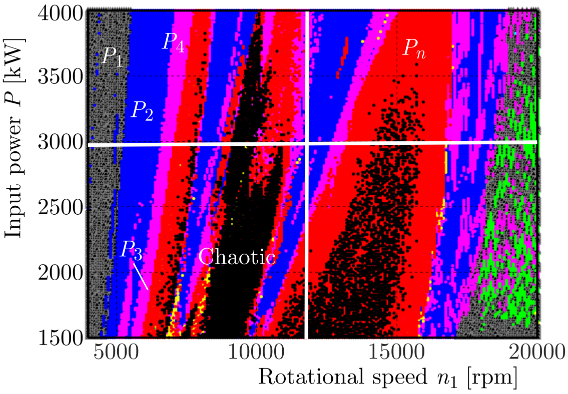

Fig. 7. Parameterized solution domain with speed and power.

The validation to the global parameterized results is carried out along the horizontal and vertical bifurcation process. In Fig. 8, these two bifurcation routes are following the white lines in Fig. 7 at 3000 kW and 11500 rpm, respectively. Evolutionary phenomena such as period doubling, chaos, as well as disturbances, is consistent with the parameterized solutions. Where the fluctuation weakens along the horizontal axis in the bifurcation diagram. Accordingly, the vibration and stability of the system could be globally predicted and improved by properly adjusting the dynamical parameters.

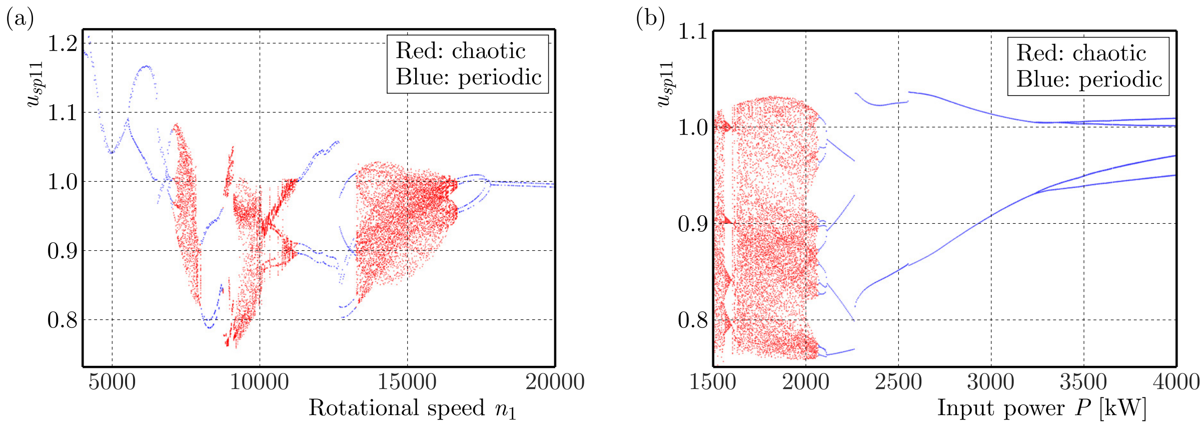

Fig. 8. Bifurcation evolution process with respect to (a) speed and (b) input power.

3.3. Fundamentals of attraction solution

The calculation of global domains associates with a couple of methods, as the continuous target parametric domain or state space are discretized into a series of cell units by the regional discretization technology combined with cell mappings. When subdividing the selected region, the reasonable number of cells can be set depending on the numerical accuracy and computational efficiency.

Define a simple cell mapping C, where the cell Z^* satisfying $Z^* = C(Z^*)$, and Z^* is called the fixed cell of the geared system, let C_m represents the cell mapping iterated m times, and C_0 refers to the self-map. If there are another cells $Z^*(j)$, $j \in \{K\}$, and K ($K \geq 2$) denotes the total amount, which satisfies the relationships:

$$Z^*(m+1) = C^m\left(Z^*(1)\right), \qquad m \in \{K-1\}, \tag{3.5}$$

$$Z^*(1) = C^K\left(Z^*(1)\right). \tag{3.6}$$

Then Z^* is said to constitute the periodic solution of period K, and each cell $Z^*(j)$ is a periodic cell with the period K. In order to strengthen the identification, such cells are called P-K cells. For example, a monocycle solution is a stable cell, which is called P_1 cell. Figure 9 exhibits a system with two periodic solutions, Z_1 is the first periodic solution with one period, Z_2, Z_3, and Z_4 finally go toward the second periodic solution with a period of 3.

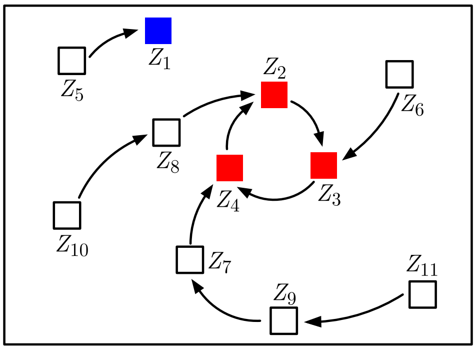

Fig. 9. Convergence of mapping cells in dynamical system.

When the initial state is discretized, the global domain of attraction with oscillation details can be computed by analyzing the evolution of cells, these computations often take a lot of time due to the 14 degrees of freedom contained in our system. Note that, if in the solutions a cell (μ^i, λ^j) shows different periodic property with its neighbors (μ^{i+1}, λ^j), (μ^i, λ^{j+1}), and $(\mu^{i+1}, \lambda^{j+1})$, that means the current cell (μ^i, λ^j) is located on the border of the domain. Hence, the above technique is able to compute the borderline of different domains as well.

3.4. Evolution behaviors of basin of attraction

3.4.1. *Global behaviors without stochasticity*

The global behaviors inside a state space reveal the vibration evolution of the system under initial conditions. Cells are calculated individually on the region of $[-1, 1] \times [1, 1]$. In Fig. 10, the state domain consists of period-2, period-4, and multi-periodic basins. The proportion of period-2 state cells in the whole domain continues to reach to 34 %, and the number of period-4 cells amount to 12393, accounting for 30 %. The period-2 basin of attraction is still expanding, and the chaotic domain has completely degenerated into the multi-periodic basin of attraction and period-4 basin of attraction, then the system is mainly covered by period-2 and period-4 basins of attraction, accounting for as high as 64 %, which further decreases the sensitivity to the initial status parameters.

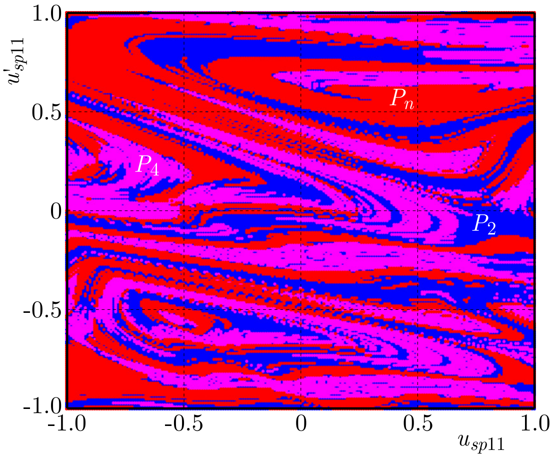

Fig. 10. Basin of attraction without stochasticity when $\xi = 0.1$.

Take the altered parameters set as $n1 = 9000\,\text{rpm}$, $\xi = 0.1$, $b = 1$. Select and verify one of the state cells at the location of $[x, \dot{x}] = [0.8, -0.07]$ (see Fig. 10). In Fig. 11, the portrait of the attractor in black is stable, while in red is still evolving. Thus, the phase trajectory and Poincaré mapping points double affirm that the responses of the system coming into period-2 state in the end, while the black dots reveal that the period-2 phase portrait has stabilized after entering a steady-state. At this point, the attractor is stable.

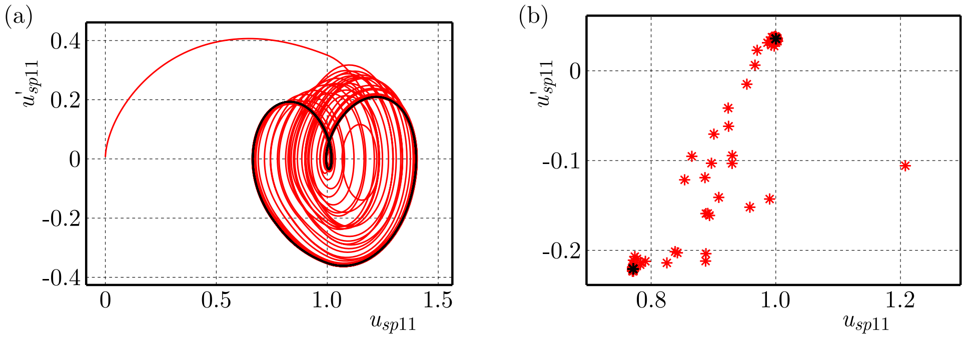

Fig. 11. Period-2 attractor without stochasticity when $\xi = 0.1$: (a) phase portrait; (b) Poincaré section.

3.4.2. Global behaviors under stochasticity

In terms of the global basins of attraction with stochasticity, which is to be compared. The basic value of the stochastic term is from the original excitation. First of all, the damping ratio ξ is selected as the stochastic parameter, and one may generate the stochastic number that corresponds to the normal distribution. Then, the necessity is to determine whether the stochastic factor η is within the upper and lower limits of the fluctuations of the analyzed parameter. Once satisfied, the stochastic number is taken as the current excitation and assigned to the parameter. If not, a normal distribution stochastic number will be regenerated again for judgment to guarantee satisfying the critical values. Subsequently, the dynamic response of the stochastic nonlinear system during meshing period is carried out.

By employing the central limit theorem (CLT) to define the meshing damping ratio ξ as a normal distribution $\xi \sim N$ (0.1, 0.00022) for a system under stochastic excitation, then ξ has the upper and lower maximum of excitations as 0.1006 and 0.0994 following the criterion of 3σ in normal distribution. Generated normal distribution of a pseudo-random damping ratio parameter could be plotted as in Fig. 12.

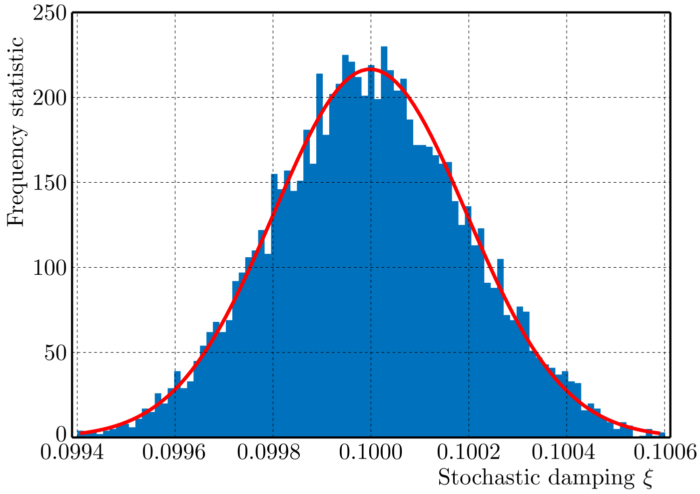

Fig. 12. Normal distribution of stochastic damping ratio.

Here, the computing formula of stochastic damping ratio ξ could be expressed as

$$\xi = 0.1 + 0.0002 \left\{ \frac{\sum\limits_{i=1}^{n} U_i - n/2}{\sqrt{n/12}} \right\}, \quad \left\{ \frac{\sum\limits_{i=1}^{n} U_i - n/2}{\sqrt{n/12}} \right\} \sim N\,(0,\ 1)\,, \tag{3.7}$$

where U_i is a uniformly distributed random number, and $U_i \sim U$ (0, 1), n represents the total amount of U_i. The global basins of attraction are calculated as shown in Fig. 13. The state domain mainly consists of period-2, period-4, and multi-period attraction domains. The proportion of period-2 attraction domain state cells in the entire space is 33%, while the proportion of period-4 and period-6 attraction domain cells is about 31%. Among them, the number of period-6 cells is 57, accounting only for 0.14%. Compared to Fig. 10, where without stochasticity on the damping ratio, although there no significant change occurs to the proportion of periodic attractors in the entire domains, due to the mutual abrupt transitions between period-2, period-4, and multi-period attractors, the number of boundary cells gradually increases, and the basin of attraction begins to turn into chaos together with more scattered period-2 cells. Additionally, a boundary between the adjacent attraction domain is suffering interference, and the vibration of the boundary cell changes frequently indicating instability. The system becomes sensitive to the initial state, and the global attraction domains develop slightly deteriorated.

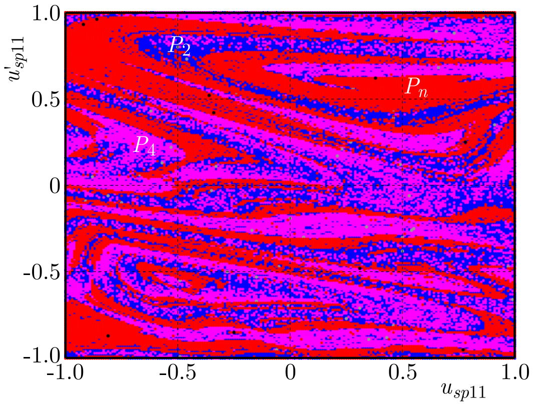

Fig. 13. Basin of attraction under stochasticity when $\xi \sim N$ (0.1, 0.00022).

The concerned state cell still at [0.8, −0.07] under stochasticity is calculated and shown in Fig. 14. From the view of structural perspective, the period-2 phase portrait and Poincaré mappings exhibit small fluctuations gradually, and it is noteworthy that the vibration of the system tends to converge towards the two fix points especially with certain oscillations on the Poincaré section in the final stage.

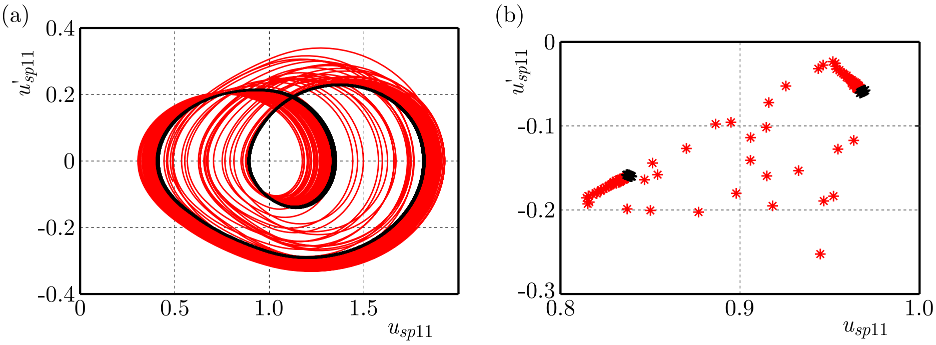

Fig. 14. Period-2 attractor under stochasticity when $\xi \sim N$ (0.1, 0.00022):
(a) phase portrait; (b) Poincaré section.

By comparing the attractors and their joint probability density distribution (Figs. 15 and 16), we found while the damping ratio is subjected to stochastic excitation, the geometric structure of the trajectory still remains in the period-2 state without much movements, but shrinks significantly in size. Meanwhile, the periodic intensity of the attractor weakens too much, and the phase portrait loosened up and dispersibility stands out. It demonstrates that stochasticity of the damping ratio could minimize the vibration stability, while their impact on the period state is not validated through this comparison.

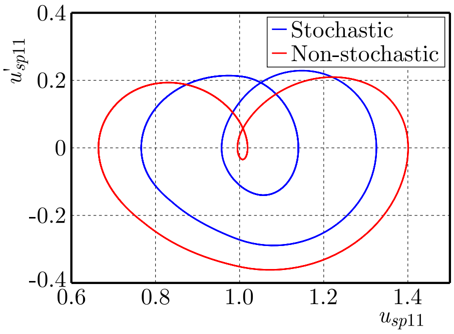

Fig. 15. Evolution transformations of period-2 attractor.

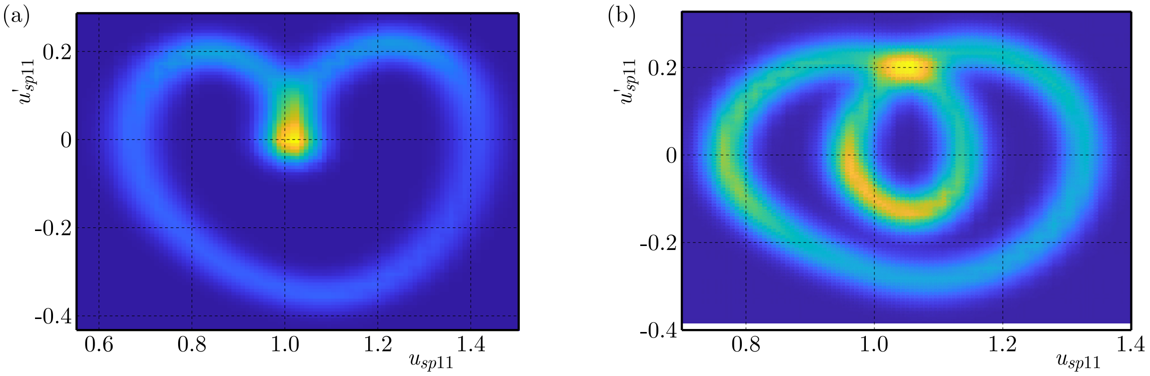

Fig. 16. Comparisons of joint probability density of period-2 attractor:
(a) without stochasticity; (b) under stochasticity.

4. Conclusions

1) A novel meshing stiffness expression approximated to a rectangular wave was proposed utilizing odd harmonic superposition, the distribution map of parameterized solution domain and the evolutions of basin of attraction subjected to two dimensional excitations were identified. The period-doubling bifurcation route was detected and verified in accordance with the bifurcation region.
2) The evolution of the geometric feature of attractors was performed associated with the joint probability density function. The phase portrait scatters during period-4 attractor going into a chaotic state, simultaneously, the Poincaré section transformed from the previous 4 point sets down to a chaotic segment fractal point groups, which causes the shift and converge occurred on attractors.
3) The global two-dimensional parameterized solution domain was calculated out, and the overall distribution patterns of periodic and chaotic cell domains on parametric planes such as speed and the damping ratio were achieved. The verification for the solution domains was confirmed correctly by means of the bifurcation diagram.
4) The period-2 attractor experienced resonance while reaching the stable state under stochastic fluctuations that in normal distribution influences on the damping ratio, the periodicity of the attractor was significantly weakened. By the comparison of the behaviors of the basin of attraction, the distributions of each periodic domain inside the overall domain keeps barely transforms, but it generates more scattered periodic cells mixed in the original domains, resulting in the deterioration of the steady-state of the system.

Acknowledgments

This work is supported by the National Natural Science Foundation of China (grant no. 51805402; 11972274), the Natural Science Foundation of Shaanxi Province (no. 2019JQ-851).

References

1. Arian, G. & Taghvaei, S. (2021). Dynamic analysis and chaos control of spur gear transmission system with idler. *European Journal of Mechanics – A/Solids*, *87*, Article 104229. https://doi.org/10.1016/j.euromechsol.2021.104229
2. Dreeben, T.D. & Pope, S.B. (1998). Probability density function/Monte Carlo simulation of near-wall turbulent flows. *Journal of Fluid Mechanics*, *357*, 141–166. https://doi.org/10.1017/S0022112097008008
3. Farshidianfar, A. & Saghafi, A. (2014). Global bifurcation and chaos analysis in nonlinear vibration of spur gear systems. *Nonlinear Dynamics*, *75*(4), 783–806. https://doi.org/10.1007/s11071-013-1104-4

4. Gou, X.F., Zhu, L.Y., & Chen, D.L. (2015). Bifurcation and chaos analysis of spur gear pair in two-parameter plane. *Nonlinear Dynamics*, *79*(3), 2225–2235. https://doi.org/10.1007/s11071-014-1807-1
5. Gyebrószki, G. & Csernák, G. (2017). Clustered Simple Cell Mapping: An extension to the Simple Cell Mapping method. *Communications in Nonlinear Science and Numerical Simulation*, *42*, 607–622. https://doi.org/10.1016/j.cnsns.2016.06.020
6. Hong, J., Yang, Z.F., Sun, B., Song, Z., & Ma, Y. (2022). Influence of local rotary inertia on the dynamic properties of rotor systems (in Chinese). *Journal of Aerospace Power*, *37*(4), 673–683. http://doi.org/10.13224/j.cnki.jasp.20210579
7. Koh, D., Anderson, R.L., & Bermejo-Moreno, I. (2021). Cell-mapping orbit search for mission design at ocean worlds using parallel computing. *The Journal of the Astronautical Sciences*, *68*(1), 172–196. https://doi.org/10.1007/s40295-021-00251-6
8. Li, Z.G., Jiang, J., Li, J., Hong, L., & Li, M. (2018). A subdomain synthesis method for global analysis of nonlinear dynamical systems based on cell mapping. *Nonlinear Dynamics*, *95*(1), 715–726. https://doi.org/10.1007/s11071-018-4592-4
9. Lin, H., Hong, L., & Liu, X. (2021). Global characteristics of solution domain and attraction domain in power split gear transmission parameter space (in Chinese). *Journal of Vibration Engineering*, *34*(2), 235–242.
10. Ma, S.C., Ning, X., & Wang, L. (2020). Dynamic analysis of stochastic friction systems using the generalized cell mapping method. *Computer Modeling in Engineering & Sciences*, *122*(1), 49–59. https://doi.org/10.32604/cmes.2020.06911
11. Marafona, J.D.M., Carneiro, G.N., Marques, P.M.T., Martins, R.C., António C.C., & Seabra, J.H.O. (2024). Gear design optimization: Stiffness *versus* dynamics. *Mechanism and Machine Theory*, *191*, Article 105503. https://doi.org/10.1016/j.mechmachtheory.2023.105503
12. Mo, S., Zhang, Y., Luo, B., Bao, H., Cen, G., & Huang, Y. (2022). The global behavior evolution of non-orthogonal face gear-bearing transmission system. *Mechanism and Machine Theory*, *175*, Article 104969. https://doi.org/10.1016/j.mechmachtheory.2022.104969
13. Saghafi, A. & Farshidianfar, A. (2016). An analytical study of controlling chaotic dynamics in a spur gear system. *Mechanism and Machine Theory*, *96*(Part 1), 179–191. https://doi.org/10.1016/j.mechmachtheory.2015.10.002
14. Tang, J.Y., Xiong, X.B., & Chen S.Y. (2011). Analysis of global character of single degree of freedom nonlinear gear system based on digraph cell mapping method (in Chinese). *Journal of Mechanical Engineering*, *47*(5), 59–65.
15. Tang, X., Bao, H.Y., Lu, F.X., & Jin, G. (2020). Nonlinear dynamic analysis of planetary gear train system with meshing beyond pitch point. *Transactions of Nanjing University of Aeronautics and Astronautics*, *37*(6), 884–897.
16. Wang, S.Y. & Zhu, R.P. (2020). Nonlinear torsional dynamics of star gearing transmission system of GTF gearbox. *Shock and Vibration*, *2020*(1), Article 6206418. https://doi.org/10.1155/2020/6206418
17. Wang, X., Jiang, J., Hong, L., Zhao, A., & Sun, J.Q. (2023). Radial basis function neural networks solution for stationary probability density function of nonlinear stochastic systems. *Probabilistic Engineering Mechanics*, *71*, Article 103408. https://doi.org/10.1016/j.probengmech.2022.103408
18. Xiang, L., Deng, Z.Q., & Hu, A.J. (2020). Dynamical analysis of planetary gear transmission system under support stiffness effects. *International Journal of Bifurcation and Chaos*, *30*(6), Article 2050080. https://doi.org/10.1142/S0218127420500807
19. Yue, X.L., Xu, Y., Xu, W., & Sun, J.Q. (2019). Probabilistic response of dynamical systems based on the global attractor with the compatible cell mapping method. *Physica A: Statistical Mechanics and its Applications*, *516*, 509–519. https://doi.org/10.1016/j.physa.2018.10.034
20. Zhang, W., Han, B.B., Li, X., Sun, J.Q., & Ding, Q. (2019). Multiple-objective design optimization of squirrel cage for squeeze film damper by using cell mapping method and experimental validation. *Mechanism and Machine Theory*, *132*, 66–79. https://doi.org/10.1016/j.mechmachtheory.2018.10.010

Manuscript received March 12, 2024; accepted for publication January 22, 2025;
published online April 22, 2025.